

# A High-fidelity Performance and Sensitivity Analysis of X-ray Pulsar Navigation in Near-Earth and Cislunar Orbits

Luke B. Winternitz,<sup>\*</sup> Munther A. Hassouneh,<sup>\*</sup> Anne C. Long,<sup>†</sup> Wayne H. Yu,<sup>\*</sup> Jeffrey L. Small,<sup>\*</sup> Samuel R. Price,<sup>\*</sup> and Jason W. Mitchell<sup>‡</sup>

Millisecond X-ray pulsars are rapidly rotating neutron stars that emit broadband electromagnetic radiation, including X-rays. These emissions can appear as pulsations to distant observers with long-term stability rivaling laboratory atomic clocks. The concept of using X-ray pulsars for navigation, commonly referred to as XNAV, has a long history in the research literature. Notably, in 2017, NASA's Station Explorer for X-ray Timing and Navigation (SEXTANT) mission, a technology enhancement to the Neutron Star Interior Composition Explorer, made a successful on-orbit demonstration of XNAV on the International Space Station (ISS) in Low-Earth-Orbit. This paper investigates the performance of XNAV in Earth and lunar regimes using a new high-fidelity XNAV analysis tool that builds on tools developed for SEXTANT and uses recent updates to the Goddard Enhanced Onboard Navigation System flight software. Specifically, we study the use of XNAV in an ISS-like orbit for comparison with SEXTANT results, in a highly-inclined geosynchronous orbit, and in an Earth-Moon L1 libration point Near Rectilinear Halo Orbit similar to that proposed for the planned lunar Gateway space station. This paper provides a high-level description of the XNAV analysis tool, baseline predicted performance results, selected sensitivity analyses, and conclusions.

## INTRODUCTION

Millisecond pulsars (MSPs) are rapidly rotating neutron stars that appear to pulsate across the electromagnetic spectrum. A subset of these MSP pulsations has long-term timing stability comparable to laboratory atomic clocks. For these pulsars, a pulsar timing model with a handful of parameters can predict the pulse arrival phase at any reference point in the Solar System to microsecond-level accuracy over months or even years. For navigation purposes, observing MSPs in the X-ray band, where some have significant (yet still faint) emissions, has certain advantages. First, X-rays are essentially immune to interstellar dispersion effects that can limit radio pulsar timing models. Perhaps more importantly, highly directional, compact, and scalable X-ray detectors can be built at relative low-cost. Directionality helps reduce background noise that can otherwise overwhelm the faint signals from MSPs. Comparing the observed phase of a pulse at a spacecraft to a prediction computed using a pulsar timing model and an estimate of the spacecraft state can provide navigation information in a manner similar to using the Global Positioning System (GPS). The concept of using observations of MSPs in the X-ray band for navigation is commonly referred to as XNAV.

The Station Explorer for X-ray Timing and Navigation (SEXTANT) mission [REF 1], a technology demonstration attached to NASA's Neutron Star Interior Composition Explorer (NICER) [REF 2] operated on the International Space Station (ISS), was, to our knowledge, the first operational mission to successfully demonstrate real-time, onboard XNAV in space [REF 3 and REF 4]. The primary objective of the XNAV analysis presented in this paper is to assess

---

<sup>\*</sup> Code 590, NASA Goddard Space Flight Center, Greenbelt, MD 20771.

<sup>†</sup> a.i. solutions, Inc, 4500 Forbes Blvd, Suite 300, Lanham, MD 20706.

<sup>‡</sup> NASA Headquarters, Washington, DC 20546.

the value of XNAV as an alternative and/or as an augmentation to state-of-the-art onboard orbit determination techniques using performance models based on NICER/SEXTANT in-flight performance and processed in the Goddard Enhanced Onboard Navigation System (GEONS) flight software (FSW) filter. This analysis builds on and significantly enhances algorithms and simulation tools developed for SEXTANT, and other tools developed for onboard navigation of space missions.

The performance benefits of onboard orbit determination using XNAV measurements are evaluated for a range of near-Earth and lunar trajectories including a LEO similar to the ISS orbit, a highly inclined geosynchronous orbit (HI-GEO), and a lunar orbit similar to the near rectilinear halo orbit (NRHO) proposed for the planned lunar Gateway space station. We note here that unlike certain notional deep space XNAV applications, the selected trajectories do not highlight the unique strengths of XNAV or provide for easy dynamic and background environments. On the contrary, the LEO, HI-GEO and NRHO trajectories are all particularly challenging for different reasons. The LEO has high dynamics and regular Earth occultations that preclude long continuous pulsar observations. The HI-GEO scenario places the detector in a harsh radiation environment resulting in extremely high background rates. The NRHO involves a three-body orbit with extreme perilune dynamics.

XNAV measurements are simulated and processed using the GEONS FSW and associated ground simulation tools available in the XNAV GEONS MATLAB Simulation (XGMS) tool suite. To support this analysis, single case and Monte-Carlo simulations of the GEONS filter are run in an open-loop mode about fixed reference trajectories provided as the truth model for XNAV measurement simulation and performance determination. XNAV measurements are simulated using models based on performance measured in the NICER/SEXTANT experiment on the ISS [REF 3 and REF 4]. Additional analyses are performed for a limited set of selected XNAV measurement configurations for each trajectory to assess sensitivity to the local clock stability and scaling up and down of the detector size.

This paper describes the XGMS simulation tool, XNAV modeling assumptions, and trajectories studied. The discussion of performance includes a discussion of the results and associated conclusions and identifies directions for future work.

## **SIMULATION ARCHITECTURE**

GEONS is a flight proven navigation software package developed at Goddard Space Flight Center (GSFC). Past and present flight heritage includes Terra, the Magnetospheric Multiscale (MMS) Mission, the Global Precipitation Measurement (GPM) Mission, and the SEXTANT mission, covering more than 20 calendar years of active flight. GEONS implements an Extended Kalman Filter (EKF) to process a variety of data types, including GPS and XNAV measurement models, and to estimate states for one or more orbiting vehicles simultaneously.

The GEONS Ground MATLAB Simulation (GGMS) tool consists of custom MATLAB simulation scripts that call methods in the GEONS FSW library to simulate measurements, process measurements, and propagate and update the state and covariance. For the analysis presented in this paper, the GEONS FSW is executed on the ground using an XNAV-enhanced version of the GGMS, referred to as the XGMS. The XGMS leverages and extends tools built for the SEXTANT mission to model the detector and signals received from XNAV MSPs and to extract navigation measurements from these signals. The XGMS includes numerous options for modeling the detector and for scheduling, simulating, and processing XNAV measurements. The measurement simulation and plotting functions are performed by a MATLAB simulation script that calls lower-level functions based on a set of configured options and interfaces to a GEONS shared library.

### **XGMS Overview and Relationship to SEXTANT Tools**

The XGMS builds on the approach to XNAV processing used for SEXTANT, which is described in [REF 5 and REF 6]. Here, the basic approach to XNAV processing consists of two interacting components: X-ray detection *event processing* and *navigation filtering*. Event processing involves collecting sets of X-ray event arrival times associated with each pulsar into observation sets and processing them into navigation measurements. In a flight system, *event filtering* is performed to discard certain events based on energy and other associated data to reject background X-rays and other noise events and optimize signal-to-noise ratio. The XGMS tool assumes that *event filtering* has already occurred.

To support high-fidelity event level simulation, the XGMS simulates the X-ray arrival process, using the standard approach of a non-homogeneous Poisson process (NHPP), i.e., a Poisson process with a time-varying arrival rate that

corresponds to the given pulsar's overall pulse shape and phase evolution [see REF 5, REF 10, REF 11, and REF 12]. After an observation interval is complete, the set of event arrival times is processed to extract an estimate of pulsar pulse phase and frequency for use in the GEONS filter navigation update.

In addition to *event processing* and *navigation filtering*, the XNAV system performance also depends critically on the specific sequence of scheduled pulsar observations. For the SEXTANT mission, scheduling of the pulsar observations was performed periodically on the ground using the NICER scheduler, although some effort was made to optimize for navigation. In this XNAV navigation study, significant effort was focused on optimizing the scheduler for navigation using an approach that would support integration into an onboard, automated system.

## **XGMS Simulation and Processing**

The first step in XNAV specific processing is to update visibility of the XNAV pulsars using a configurable pulsar observation schedule replanning time horizon. For example, for a LEO simulation, replan could occur every 6 hours. When the replan is due, both the truth and estimator states are forward propagated for 6 hours and visibility to each active XNAV pulsar is determined. Sun, Earth, Moon, Mars, Jupiter, and Venus are all checked for occultations and additional keep-out zone (KOZ) constraints that require the angle between the vectors from the detector to a pulsar and from the detector to each celestial body to be greater than the KOZ angle set for each body. In addition, the particle-induced X-ray background radiation is determined along the truth and estimator trajectory and a configurable threshold on the background radiation is used to exclude XNAV observations in regions of high background. The estimator's visibility is provided as an input to the schedule planner, which operates on the same replanning horizon. Thus, every 6 hours in our LEO example, a schedule of observations of a sequence of pulsars is determined for the next 6 hours.

Note that under the current assumptions, pulsars are viewed sequentially one-at-a-time. Multiple scheduling algorithms were implemented and tested. Different schedulers proved to outperform others for the various cases studied, and others could have strengths for other orbits, or for real-world operations, etc. After the schedule is determined, the next step in the simulation is to update the per-pulsar observation time (or *obstime*) table. These tables keep track of accumulated observation time on each pulsar. Each pulsar has a target amount of observation time (e.g., 1800s) required before a measurement will be generated. During this update, the current XGMS propagation interval increment (e.g., 60s) is added to the time of the pulsar currently being observed.

When the observation target time is reached, the measurement generation process is triggered. After the *obstime* update, the X-ray events for the current pulsar and propagation interval are simulated and added to the associated pulsar *event buffer*, a per-pulsar data structure containing the X-ray arrival times and associated data for a given observation. X-ray event simulation involves simulating the arrival times of the NHPP associated to the pulsar of interest. In the event level simulation used in this study, a multi-level optimization process is implemented to process the events in the relevant event buffer to compute a phase and frequency measurement. Finally, the phase and frequency measurements are provided to the GEONS filter for incorporation into a state update. The following subsections discuss these processes in more detail.

## **Particle Background Radiation Models**

Background radiation contributes to the level of noise in the XNAV phase and frequency measurements. High levels of background radiation can prevent the detection of MSP pulsations and thus acquisition of useful measurements, effectively rendering the MSP not visible. The background radiation level at the detector is a function of pulsar source radiation and non-pulsar source radiation, which includes radiation induced by the local particle background. This particle background consists primarily of trapped electrons and protons at LEO and HI-GEO and solar galactic cosmic flux (GCF) and solar wind in high altitude orbits, cislunar space, and interplanetary orbits. The source background levels depend on where the detector is pointing and does not depend on the detector location, while the particle background depends strongly on the orbit and location within it. Source background terms are well understood based on NICER preflight and on-orbit data and can be used in simulations in other orbital regimes assuming a NICER-like detector; however, the particle background must be modeled based on the orbital regime.

To get a rough estimate for the particle background for a NICER-like detector in different orbital regimes, the SPENVIS tool [REF 7] was used to calculate the particle background flux at a grid of latitudes and longitudes at LEO, HI-GEO and Lunar altitudes (408 km, 35,786 km, and 384,400 km, respectively). The AE8/AP8 particle model [REF 8 and REF 9] provides electron and proton flux (in units of counts/second/cm<sup>2</sup>) over a range of energies. We integrated the flux over energy using a lower cutoff threshold of 0.3 MeV for electrons and 30 MeV for protons and no upper

cutoff. To scale and convert this integrated flux into particle counts per second seen by a NICER-like detector, a linear model was fit using NICER mission data from the 0.4-2.0 keV band shown on the left plot in Figure 1. This figure is a heatmap where the brightness corresponds to the particle background level in counts per second. The key features of the radiation environment for the NICER LEO are the South Atlantic Anomaly (SAA) in the lower center of the figure and the polar horns, which are the top left and bottom right parts of the figure.

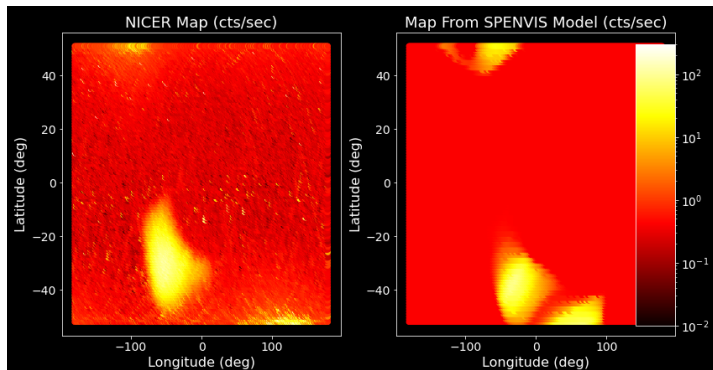


**Figure 1. NICER Particle Background Map vs. SPENVIS Model**

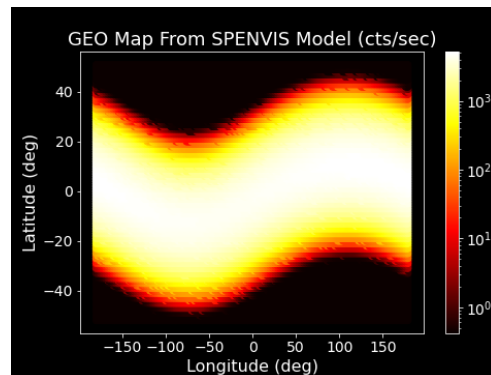


**Figure 2. GEO Background Map**

The background map from this model is shown in the right plot in Figure 1. There is a noticeable offset between the SAA and polar horns, which is expected since the positions of each vary based on a variety of factors. To exclude this difference, only a segment of the NICER data around the SAA was used to fit the model and the SPENVIS data was shifted to better correlate with the NICER data. After this model is applied, the mean pulsar source background is subtracted from the computed background to isolate the particle background component since the NICER data contains both source and non-source radiation.

The particle background in GEO is greater in magnitude and extent compared to LEO. Figure 2 shows the GEO particle background map computed using SPENVIS with the linear SPENVIS model. Under such high background levels in the radiation belt that spans  $40^\circ$  in latitude on either side of the equator, MSP pulsations can require impractically large observation times for detection, and thus XNAV measurements can become unavailable or extremely sparsely available. Furthermore, the current computational algorithms used in the XGMS are not well-equipped to handle simulation and processing of high-count rate observations. Therefore, equatorial, and low inclination Geostationary orbits are not expected to be practical candidates for application of XNAV. In this study, we limit MSP observations to regions with low to moderate background levels and for the geosynchronous orbit analysis consider only HI-GEO orbits that spend enough time above about  $40^\circ$  of the equator to accumulate enough high-quality XNAV measurements for nominal navigation performance. However, we leave open the possibility that XNAV in low inclination GEO orbits could be enabled through special techniques, see Future Work section for a brief discussion of operation in regions of high background.

Along with the *baseline* GEO map created using a 0.3 MeV and 30 MeV threshold in SPENVIS for the electron and proton flux respectively, a more *optimistic* GEO background map was created by raising the electron energy threshold to 3 MeV. This assumption could be consistent with a GEO spacecraft using XNAV having more radiation shielding than NICER. The optimistic map reduces the width of the GEO radiation bands and allows for XNAV observations to be taken over a larger portion of the orbit. We used this more optimistic GEO map in the analysis of this paper but there is uncertainty about which map is more realistic.

The particle background for the NRHO is assumed to be constant throughout the trajectory since the orbit is outside of the Earth's trapped particle radiation belts and the radiation mainly comes from solar particles, although the level of these particles will change according to the solar cycle and during transient solar flare events, which were not modeled. Passing the SPENVIS output for the NRHO through the linear model gives a constant background of around  $\sim 0.34$  counts per second, which is somewhat larger than the nominal NICER average LEO particle background. This is physically plausible since LEO is partially shielded from the solar wind and GCF by the Earth's magnetic field.

### Pulsar Observation Scheduling Algorithms

Due to the faint nature of the available MSPs and the properties of a NICER-like detector, it is necessary to observe each MSP for periods ranging from several minutes to several hours or more to generate a single measurement. The

sequencing of these relatively sparse measurements can have significant effect on performance; therefore, the XGMS scheduling algorithms attempt to optimally design the observing plan by choosing schedules that most reduce the semi-major axis variance associated to a state correction. The results below use only two of several XGMS schedulers: either *DP2*, a dynamic programming-based algorithm, or *bestrand*, which chooses the best of a large number of randomly generated feasible schedules.

### Observation Time Tracking and Event Simulation

Following SEXTANT [REF 5] and references [REF 10, REF 11, and REF 12], the X-ray detection events generated by observing a given pulsar are modelled as the arrival times of a NHPP whose rate is given by the pulsar pulse evolution, i.e., the time variation of the X-ray flux, as seen at the detector. The pulse evolution can be separated into a fixed pulse shape and a phase evolution model.

XNAV pulsar pulse evolution models are needed to simulate this process. For this analysis, we use the SEXTANT pulsar almanac entries for the five best known XNAV MSPs (not including the exceptional Crab Pulsar). The pulsar almanac provides all relevant parameters necessary to determine the pulse evolution, including a normalized pulse shape with associated signal and background count rate parameters (for a NICER-like detector), and a phase evolution or *timing model*. The XGMS timing models make use of the pulsar timing software TEMPO2 [REF 13] and are specified in the almanac as a set of TEMPO2 model parameter sets. These are preprocessed (using TEMPO2) and provided to the XGMS simulation as sets of piecewise continuous polynomial coefficients that are evaluated within the XGMS to compute pulse phase and frequency at a given time, at a reference observatory taken to be at the center of the Earth. The pulse templates are given as pulse phase profile for each pulsar over one cycle. Examples can be seen in Figure 3.

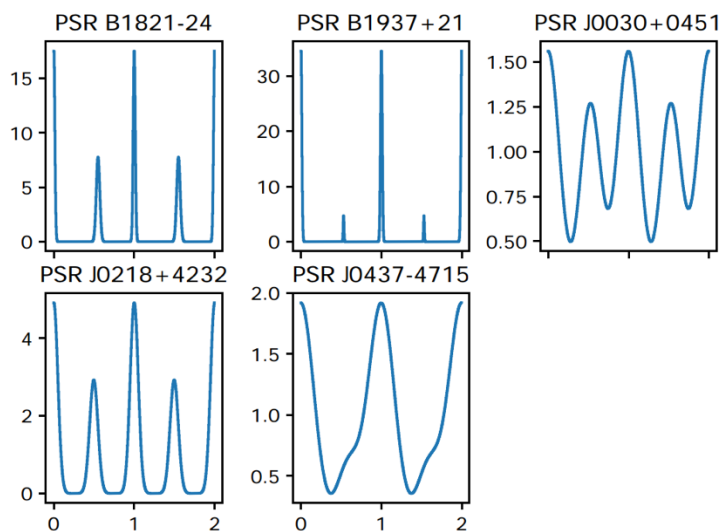


**Figure 3. Pulse Shapes of the Five MSPs Used in this Analysis. Two Cycles of Each Pulsar are Shown (Reproduced from [REF 3])**

The count rates give nominal signal counts and background counts separated into un-pulsed, other sources, diffuse, and particle background components. The almanac particle background corresponds to an estimate of the NICER nominal particle background and must be modified in the simulation to accurately model the particle background evolution along the desired simulation trajectory. Given a model for the pulse evolution at the detector, it is straightforward to generate samples of an NHPP that have this pulse as its rate. The XGMS uses an updated accept/reject approach that has some improvements over one of the methods used for SEXTANT and can run on-the-fly. Timing errors consistent with our local clock model are added to the true event arrival times to generate the biased arrival times available to the event processing algorithms.

Pulsar events must be collected over an observation time interval sufficient to provide enough photons to generate a measurement before moving from the event processing to measurement generation. Pulsar B1937+21 has a lower signal count rate (and signal to noise ratio) than the other MSPs and thus requires a longer observation time to make reliable measurements. In this study, the target times were set empirically and were not carefully optimized. The

measurement noise level is related to the Cramer-Rao Lower Bound (CRLB) associated with estimating NHPP phase and frequency (or phase and frequency correction) parameters and derived in [REF 14] and in the context of XNAV in [REF 10, REF 11, and REF 12]. Since we use a maximum likelihood approach, we can expect to achieve the CRLB asymptotically (for large enough set of photons).

In this study, we consider scaling the detector size (effective area) up and down. The assumption is that scaling the detector size by a given factor  $S$  will scale the signal and background count rates by the same factor. For example, when scaling down the detector size, we correspondingly scale up target observation time by the same factor to maintain a constant expected number of events, and vice-versa. The theoretical phase measurement noise variance (CRLB) has the form of a constant that depends only on the signal-to-total-count-rate (constant under the scaling) times the inverse total count rate, times the inverse observation-time. Thus, the phase measurement noise is constant under a detector size scaling. However, we can have measurements  $S$  times as often with an  $S$  times bigger detector; therefore, the filter should obtain a phase measurement noise variance reduction proportional to  $S$  (by averaging). The frequency measurement variance has the same form as phase, except it is proportional to the observation time to the minus third power, rather than just inverse observation time. Therefore, the frequency measurement noise *decreases* for a scaled down detector when increasing the observation time by the same scaling factor, even after accounting for the filter's effective averaging of measurements.

## Event Processing Algorithms

When an *obstime* target is reached and the associated events simulated, the *event buffer* is ready for processing into a measurement. First, a predicted phase is associated with each X-ray event time by evaluating the pulsar timing model at the detector using the filter's predicted position/velocity/clock states. This method obtains state predictions by back propagating from the current time. Next, an optional coarse background estimate is determined for use in the estimation. Then, a linear correction to the predicted phases is computed via a Maximum Likelihood approach, as used in SEXTANT. See [REF 5 and REF 6] for details, and earlier references [e.g., REF 10, REF 11, and REF 12]. This proceeds by a grid search that is constrained by the a priori uncertainty of the correction model parameters. The output of the grid search is then used to initiate an optional continuous optimization of the likelihood function to refine the estimate and optionally estimate auxiliary parameters (including an additional quadratic correction parameter and count rate estimates). Next, a rejection test is implemented based on the result of the optimization to attempt to limit measurement outliers. Finally, phase and frequency measurements are constructed based on a predicted phase and frequency and the estimated correction model.

## XNAV SIMULATION ASSUMPTIONS

The baseline XNAV assumptions used in this study include:

- Single detector with characteristics based on a nominal NICER 56-concentrator detector, scalable via a *number-of-concentrators* (area) parameter
- SEXTANT *post-flight* updated pulsar almanac (~2018) for five key XNAV MSPs: PSR\_B1821-24, PSR\_B1937+21, PSR\_J0218+4232, PSR\_J0030+0451, and PSR\_J0437-4715
- Visibility constraints:
  - Sun <45° baseline (we also consider a 35° constraint, which keeps PSR B1937+21 visible all year)
  - Earth<30°, Moon <15°, Planets <1°
  - Particle rate < 0.8 counts/s
- Particle background models
  - NICER-based particle map for LEO
  - *Optimistic GEO* particle SPENVIS-based particle background maps for HI-GEO
  - Constant SPENVIS-based GCF map for NRHO giving ~0.34 counts/s
- Baseline simulations start October 1 running up to 39 days, which provides good visibility to MSPs
- Detector referenced to space atomic clock modeled based on a commercially available Rubidium Atomic Frequency Standard (RAFS)

The clock simulation model uses a twice integrated white noise model. The variances of the driving white noises processes are obtained by fitting this model to the RAFS typical performance data presented in REF 16. In addition,

performance using an MMS-like Ultra-stable Oscillator (USO) is investigated as part of the clock sensitivity analysis. Figure 4 shows the Hadamard deviation for each of these oscillators.

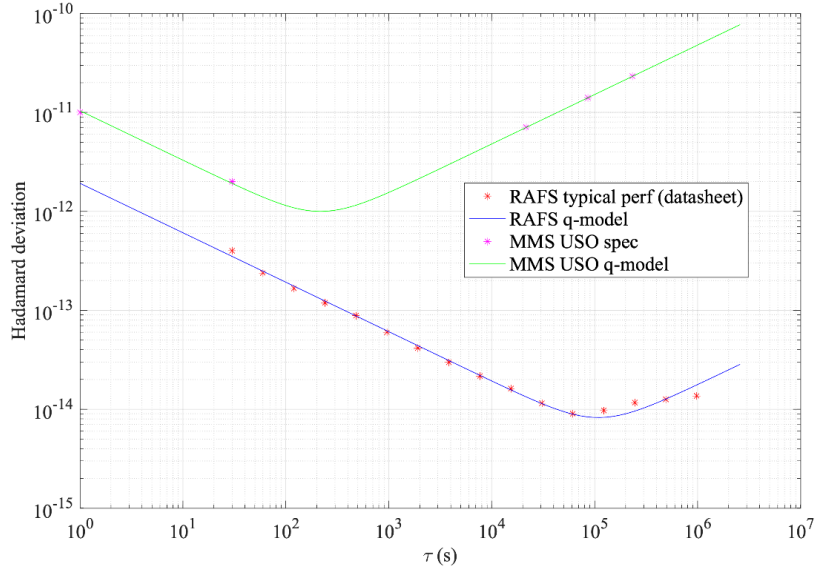


**Figure 4. Master Oscillator Stability**

## NAVIGATION ANALYSIS

This section presents the results from an evaluation of XNAV performance for four mission scenarios: an ISS-like space station in a LEO, a spacecraft in a HI-GEO orbit, and a Gateway-like space station in an NRHO. The truth trajectories are simulated in GEONS using high-fidelity dynamic models. Lower-fidelity dynamic models are used in the GEONS filter processing to simulate dynamic modeling errors. Monte-Carlo simulations are performed for each of the baseline trajectory configurations. In addition, we investigated sensitivity to clock stability considering the baseline RAFS clock, a reduced quality USO, and the possibility of a perfect or independently disciplined clock (no clock). In the no clock case, we do not add timing errors to the detected event time stamps and do not estimate clock error states in GEONS. Sensitivity to detector size is also investigated, considering a detector with 7, 14, 28, 56, and 112 concentrators.

To start the navigation process, the GEONS filter requires an initial state estimate and covariance. The simulations with a baseline 56-concentrator detector are initialized with a basic initialization state with initial errors vs. truth consistent with expected accuracy after insertion into mission orbit and a covariance matrix that is diagonal with off-diagonal terms to account for typical orbital correlations between radial position and in-track velocity and between in-track velocity and radial position. In the simulations where the detector size is scaled down, it was determined that an improved initial state and covariance is needed to achieve stable solutions. For this reason, all detector sensitivity simulations are run using increased orbital correlations, and more consequentially, with limited Deep Space Network (DSN) ground station (GS) tracking contacts added at the start of the simulation, with the exact schedule adapted for each of the three orbit cases studied. We refer to this as the *gsinit* initialization to distinguish it from the basic initialization method. The *gsinit* procedure is intended to emulate initialization of the onboard filter using an uploaded state and covariance that is determined on the ground by processing DSN radiometric measurements. The *gsinit* initialization approach results in much faster filter convergence than with the basic initialization method used in the baseline simulations. The *gsinit* DSN tracking model used optimistic noise settings, but steady-state results were not sensitive to a change to more conservative values. A nominal per-pass range bias was also modelled.

In each of the 70 Monte Carlo trials, the following error parameters are varied based on random seeds:

- Initial position, velocity, clock bias, clock bias rate, clock bias acceleration, area, mass, solar radiation pressure coefficient, and atmospheric drag coefficient (only for LEO) errors based on the initial covariance
- Detector truth clock bias, clock bias rate, and clock bias acceleration states
- True NHPP arrival times for *event simulation* mode

- XNAV phase and frequency noise errors for *measurement simulation* mode
- Orbit maintenance maneuver (OMM) errors and momentum unload (*desat*) residual delta-Vs for the NRHO trajectory

The following sections include plots showing the results of the Monte Carlo simulations. In these plots, the root-sum-square (RSS) position and velocity errors for each of 70 Monte Carlo trials are plotted in grey and 3-times the average estimated RSS root-variance at each time step is plotted in green.

### XNAV Simulation and Navigation Performance Results for LEO Trajectory

This section evaluates XNAV for navigation of an ISS-like space station in a 400 km altitude circular orbit, which is similar to the orbit of the NICER/SEXTANT experiment. This LEO trajectory is challenging due to the high dynamics and regular Earth occultations that preclude long continuous pulsar observations. Table 1 lists the modeling used for the truth trajectory and the onboard navigation filter for all LEO simulations. The velocity process noise variance rate is tuned to achieve a realistic covariance that aligns with the observed errors. Figure 5 shows the direction of the pulsars with respect to the LEO trajectory.

**Table 1 Environment Models for the LEO Configuration**

	Truth Trajectory	GEONS Filter
<b>Point Mass Gravity</b>	Sun, Moon, Venus, Mars, Jupiter	Sun, Moon, Venus, Mars, Jupiter
<b>Earth Gravity Model</b>	30x30 EGM96	25x25 EGM96
<b>Atmospheric Drag</b>	Spherical $C_D=2.2$	Initial $C_D=2.2 \pm 30\% 3\sigma$ Correction to $C_D$ is estimated
<b>Mass</b>	400000 kg	400000 kg $\pm 1\% 3\sigma$
<b>Area</b>	1000 m <sup>2</sup>	1000 m <sup>2</sup> $\pm 10\% 3\sigma$
<b>Propagation Step</b>	10 s	10 s

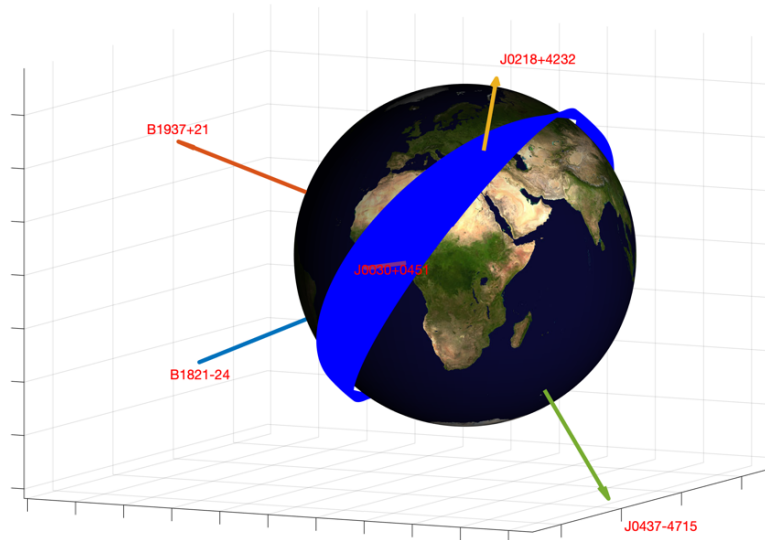


**Figure 5. Pulsar Orientation for LEO**

#### Baseline Processing Results for LEO

The *DP2* scheduler was used for the LEO runs. The estimated states are the LEO position, velocity, clock bias, clock bias rate, clock acceleration, and correction to the atmospheric drag coefficient. The baseline, nominal detector size LEO simulations are initialized using a basic initialization, with the initial state errors randomly computed based on the following variances and off-diagonal correlation coefficients, which are consistent with a low-fidelity ground-

based initial solution and is similar to the initialization approach used for SEXTANT ground simulations and experiments:

- RIC Position Variances:  $1000^2$  meters<sup>2</sup> each axis
- RIC Velocity Variances: 1 meters<sup>2</sup>/sec<sup>2</sup> each axis
- Clock Bias Variance:  $10000^2$  meters<sup>2</sup>
- Clock Bias Rate Variance:  $10^2$  meters<sup>2</sup>/sec<sup>2</sup>
- Clock Bias Acceleration Variance:  $(3 \times 10^{-7})^2$  meters<sup>2</sup>/sec<sup>4</sup>
- Atmospheric Drag Coefficient Correction Variance:  $(0.22)^2$
- Correlation of R Position and I Velocity: -0.95
- Correlation of I Position and R Velocity: -0.90

Figure 6 shows visibility of the MSPs and associated pulsar measurements during the simulation time span.

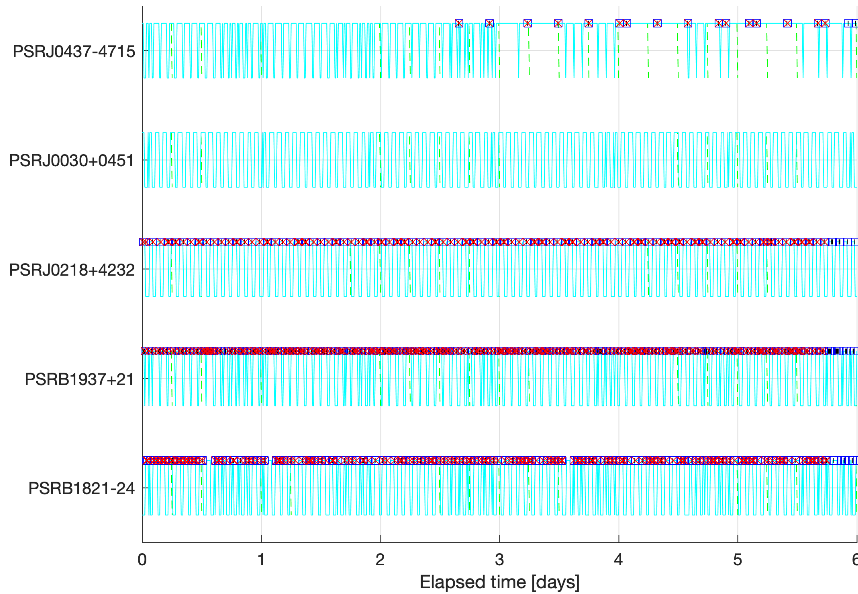


**Figure 6. LEO visibility showing regular Earth occultations (~16/day) for an example run. The cyan line indicates visible/not visible pulsar (high=visible), red marks indicate applied measurements, and blue squares indicate planned measurements.**

Figure 7 shows the RSS position and velocity and clock bias and bias rate performance for the set of 70 Monte Carlo trials for the baseline configuration with a RAFS quality clock. The RSS position and velocity estimates require about 4 days to converge to steady-state errors below 10 km and 10 m/s, consistent with SEXTANT simulations and onboard results. The clock bias converges quickly requiring less than 1 day to reach steady state errors below 3 km, whereas the clock bias rate is still converging after 6 days of processing to below 0.02 m/s with RAFS.

#### *Sensitivity Analysis Results for LEO*

Monte Carlo simulations were run to evaluate the sensitivity of XNAV performance for the LEO trajectory to clock quality (USO, RAFS, no clock). The resulting steady-state performance results indicate that the RSS position and velocity performance are not degraded when the less stable USO is used versus the baseline RAFS clock; however, the clock bias errors are about 10% larger and clock rate errors are about 2.5 times larger with the USO. Comparison of RAFS performance versus the no clock results indicate that RAFS-related errors are not the primary error source in the position and velocity errors.

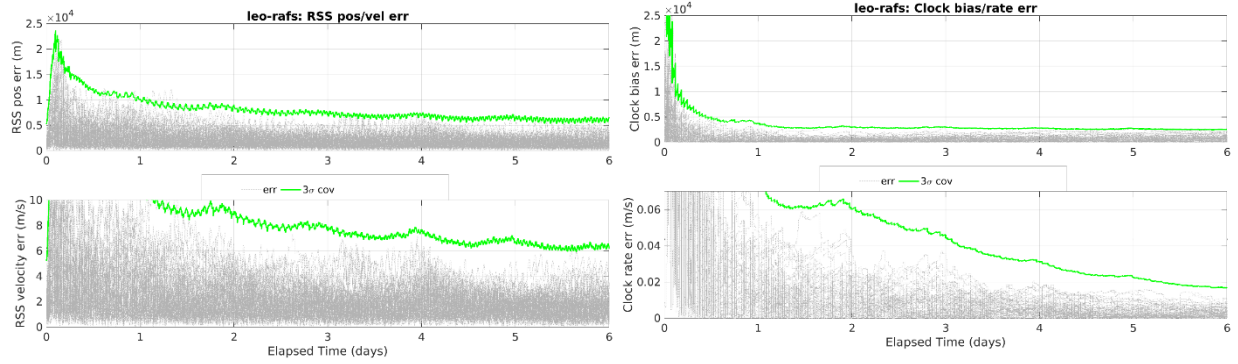


**Figure 7. XNAV RSS Position and Velocity Errors (left) and Clock Bias and Rate Magnitude Errors (right) for LEO Baseline Configuration**

Monte Carlo simulations were run to evaluate the sensitivity of XNAV performance for the LEO trajectory to detector scaling (7, 14, 28, 56, 112 concentrators). These simulations, which were run over a longer 12-day time span, used a *gsinit* initialization procedure, including one 4-hour DSN tracking contact at the start of the simulation and higher orbital correlations between radial position/intrack velocity and intrack position/radial velocity. The detector size sensitivity results indicate that performance is very sensitive to the detector size. Acceptable performance is achieved starting with the 28-concentrator detector; however, most of the 7-concentrator solutions diverged and the 14-concentrator solution is not very stable.

### XNAV Simulation and Navigation Performance Results for HI-GEO Trajectory

This section evaluates XNAV for navigation of a satellite in a highly inclined geosynchronous circular orbit. The geosynchronous scenario is challenging because it places the detector in a harsh radiation environment resulting in extremely high background rates. However, the HI-GEO trajectory spends a significant fraction of time outside the radiation belts. Note that equatorial and low inclination Geostationary orbits are not expected to be practical candidates for application of XNAV.

The HI-GEO truth trajectory is generated in GEONS by propagating an initial state vector for a nearly circular geosynchronous orbit at a  $75^\circ$  inclination. Table 2 lists the modeling used for the truth trajectory and the onboard navigation filter for the HI-GEO configuration. The velocity process noise variance rate is tuned to achieve a realistic covariance that aligns with the observed errors. Figure 8 shows the direction of the pulsars with respect to the HI-GEO trajectory.

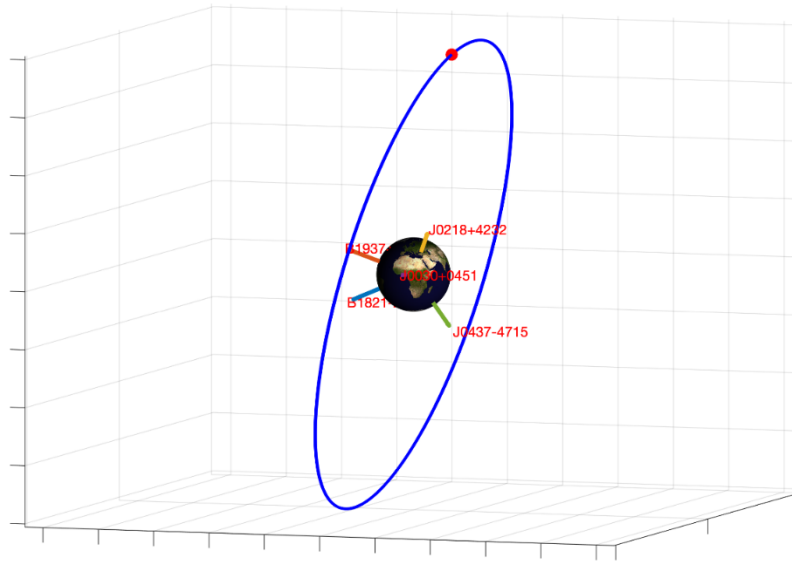
**Table 2. Environment Models for HI-GEO Configuration**

	Truth Trajectory	GEONS Filter
<b>Point Mass Gravity</b>	Sun, Moon, Venus, Mars, Jupiter	Sun, Moon, Venus, Mars, Jupiter
<b>Earth Gravity Model</b>	30x30 EGM96	10x10 EGM96
<b>Solar Radiation Pressure</b>	Spherical $C_R=1.2$	Initial $C_R=1.2 \pm 30\% 3\sigma$
<b>Area</b>	50 m <sup>2</sup>	50 m <sup>2</sup> $\pm 10\% 3\sigma$
<b>Mass</b>	5000 kg	5000 kg $\pm 1\% 3\sigma$
<b>Propagation Step</b>	60 s	60 s

#### Baseline Processing Results for HI-GEO

The simulations are run using the trajectory models provided in Table 2. XNAV observations are scheduled using the *DP2* scheduler. The estimated states are the HI-GEO position, velocity, solar radiation pressure coefficient correction, clock bias, clock bias rate and clock bias acceleration. Initialization of the baseline, nominal detector size HI-GEO simulations uses a basic initialization, with the initial state errors randomly computed based on the following variances and off-diagonal correlation coefficients:

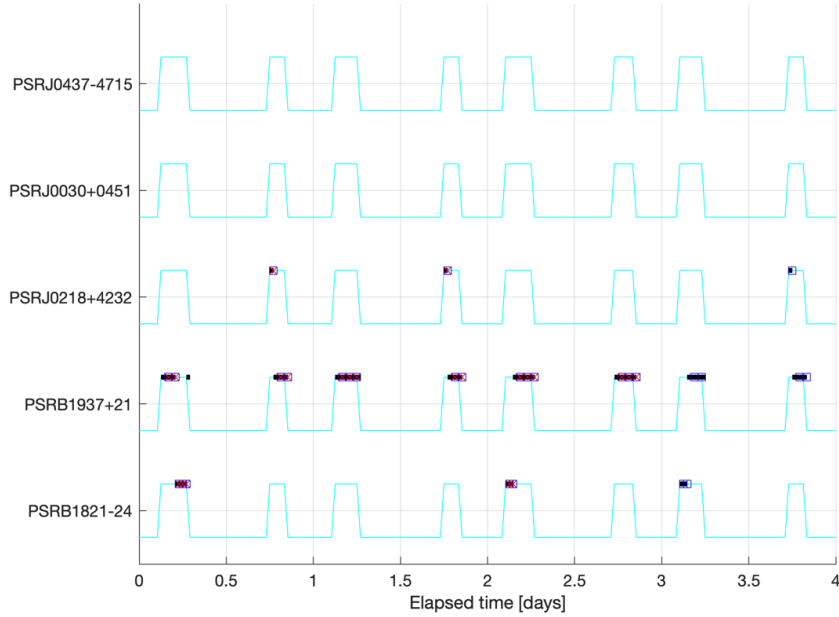
RIC Position Variances:  $1000^2$  meters<sup>2</sup> each axis  
 RIC Velocity Variances:  $0.1^2$  meters<sup>2</sup>/sec<sup>2</sup> each axis  
 Clock Bias Variance:  $10000^2$  meters<sup>2</sup>  
 Clock Bias Rate Variance:  $1^2$  meters<sup>2</sup>/sec<sup>2</sup>  
 Clock Bias Acceleration Variance:  $(3 \times 10^{-7})^2$  meters<sup>2</sup>/sec<sup>4</sup>  
 Solar Radiation Pressure Coefficient Variance:  $(0.12)^2$   
 Correlation of R Position and I Velocity: -0.95  
 Correlation of R velocity and I position: -0.90



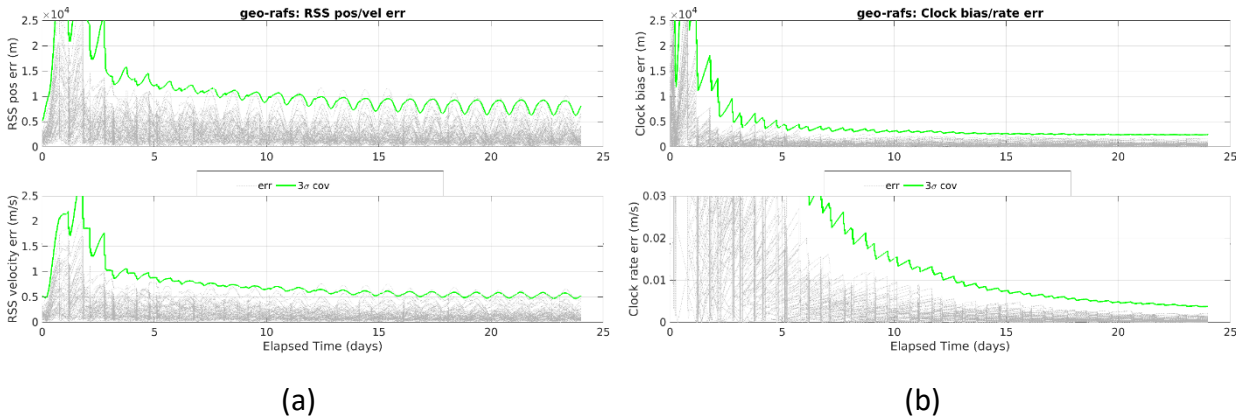
**Figure 8. Pulsar Orientation for HI-GEO**

Figure 9 shows the associate visibility (high = visible) and scheduled observations and measurement times (marks on the visibility lines) based on the *optimistic GEO* background map. Note that two pulsars provide the majority of the measurements with most of the XNAV measurements coming from pulsar B1937+21, which provides the most accurate measurements: this is a typical schedule behavior when using the *DP2* scheduler.

Figure 10 (a) shows the RSS position and velocity performance for the set of 70 Monte Carlo trials for the baseline HI-GEO configuration with a RAFS quality clock. The RSS position and velocity require about 15 days to converge to steady-state performance levels with maximum errors below 10 km and 1 m/s, respectively. Figure 10 (b) shows the corresponding clock bias and clock bias rate performance with steady-state errors below 2 km and 0.005 m/s. The clock bias converges to steady-state performance in about 15 days, whereas the clock bias rate has not fully converged by the end of the simulation time span. The “sawtooth” character of the clock errors can be attributed to error growth during gaps in measurement availability when periodically passing through high background regions in the radiation belts; this effect is much more pronounced in the case of the less stable USO clock described in the next section. The variation in the position and velocity errors has the orbital period and could be associated with periodic changes in the geometry of the XNAV measurements.



**Figure 9. HI-GEO visibility with observations and measurement times showing the periodic loss of visibility when passing through radiation belts and how observations and measurements must be scheduled only during periods of visibility. Cyan line indicates visible/not visible pulsar (high=visible), red marks indicate applied measurements, and blue squares indicate planned measurements.**



**Figure 10. RSS Position and Velocity Errors (left) and Clock Bias and Rate Magnitude Errors (right) for HI-GEO Baseline Configuration**

### Sensitivity Analysis Results for HI-GEO

Monte Carlo simulations to evaluate the sensitivity of XNAV performance for the HI-GEO trajectory to the variations in clock stability (USO, RAFS, no clock) indicate that the RSS position and velocity steady-state errors are about 10% larger, the clock bias error are about 50% larger and the clock rate errors are about 15 times larger when the less stable USO is used versus the RAFS clock. Comparison of RAFS performance versus the no clock results indicate that RAFS-related errors are not the primary error source in the position and velocity errors.

Monte Carlo simulations were run to evaluate the sensitivity of XNAV performance for the HI-GEO trajectory to detector scaling (7, 14, 28, 56, 112 concentrators) using a *gsnit* initialization procedure with two 4-hour DSN tracking contacts separated by 12 hours at the start of simulation. Except for the 7-concentrator case which is not stable, these results indicate that smaller detectors provide comparable performance down to a 1/4 size detector (14 concentrators) and a 2x (112 concentrator) detector provides only a marginal improvement. Monte Carlo simulations were run to

evaluate the sensitivity of XNAV performance for the HI-GEO trajectory to inclination (45° to 90°) using a nominal 56-concentrator detector and the basic initialization procedure. These results indicate that performance is significantly degraded for inclinations below 65°, where high particle background rates reduce visibility significantly. The convergence time and steady-state errors decrease gradually as the inclination increases from 65° to 90°.

### XNAV Simulation and Navigation Performance Results for NRHO Trajectory

This section evaluates XNAV for navigation of a lunar space station in an NRHO. This is the orbit planned for NASA’s Lunar Gateway. The NRHO trajectory is challenging because it involves a three-body orbit with extreme perilune dynamics.

The NRHO configuration is based on a conceptual model of a proposed lunar Gateway space station with

- Plausible mass and a Sun-pointed attitude
- Once-per rev Orbit Maintenance Maneuvers (OMMs) near apolune with magnitudes of 0.025 m/sec ( $1\sigma$ )
- Additional disturbances to model momentum desaturation burns (*desats*) at known times
  - 2 *desats* near perilune and 1 *desat* 1 day prior to OMM
  - Magnitudes of 0.0025 m/s ( $1\sigma$ ) in random directions

The orbital truth data is generated in GEONS by propagating an initial state vector extracted from a 15-year reference trajectory for the Gateway orbit available from NASA’s Navigation and Ancillary Information Facility (NAIF) [REF 18], which is an Earth-Moon L2 southern NRHO with average periapsis altitude ~1800 km, apoapsis altitude of 68,000 km, 6.5-day period, in 9:2 resonance with the Moon’s orbit. Figure 11 shows the GEONS propagated truth trajectory in an Earth-Moon rotating frame.

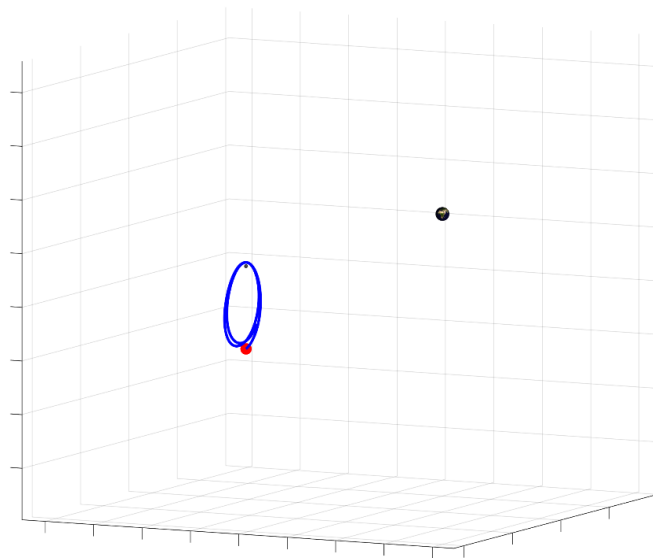


**Figure 11. NRHO Truth Reference Trajectory in an Earth-Moon Rotating Frame. Earth is the big sphere, moon is the smaller sphere, and the red dot is the spacecraft.**

Table 3 lists the modeling used for the truth trajectory and the onboard navigation filter for the NRHO configuration, where the model used in the truth trajectory includes impulsive OMM knowledge errors, and *desat* residual delta-Vs.

**Table 3. Environment Models for NRHO Configuration**

	<b>Truth Trajectory</b>	<b>GEONS Filter</b>
<b>Point Mass Gravity</b>	Sun, Earth, Venus, Mars, Jupiter	Sun, Earth, Venus, Mars, Jupiter
<b>Lunar Gravity Model</b>	16x16 GRGM900C	8x8 GRGM900C
<b>Solar Radiation Pressure</b>	Spherical $C_R= 1.2$	Initial $C_R= 1.2 \pm 30\% 3\sigma$ , Coefficient estimated
<b>Area</b>	250 m <sup>2</sup>	250 m <sup>2</sup> $\pm 10\% 3\sigma$
<b>Mass</b>	25000 kg	25000 kg $\pm 1\% 3\sigma$
<b>OMM Execution Error</b>	0.75 mm/s fixed, 0 deg direction, 1% magnitude ( $3\sigma$ ) based on random 7.5 cm/s reference OMM ( $3\sigma$ )	Velocity process noise added as defined below
<b>Residual <i>desat</i> Delta-V Magnitude</b>	0.0075 m/s ( $3\sigma$ ) in random direction	Velocity process noise added = $(0.5*0.0025 \text{ m/s})^2$
<b><i>desat</i> Schedule</b>	<ul style="list-style-type: none"> <li>- 1 hr prior to OMM (MA=179 deg)</li> <li>- 2 between -20 and 20 deg. true anomaly</li> </ul>	
<b>Propagation Step</b>	60 s	60 s

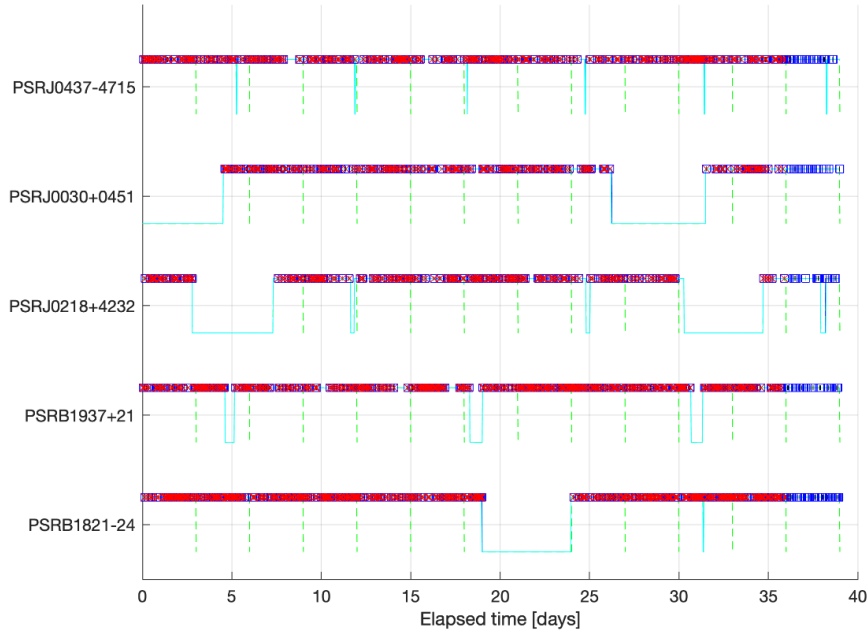
The velocity process noise model used for the NRHO configuration increases near perilune as (the ratio of the distance to apolune over the current slant range distance to the Moon) and returns to the nominal value near apolune to accommodate lunar gravity errors, which are largest at perilune. The process noise variance rate is tuned to achieve a realistic covariance that aligns with the observed errors and improve the errors at perilune. Short velocity process noise increments are added to each component to compensate for *desat* errors and to compensate for OMM delta-V knowledge errors.

*Baseline Processing Results for NRHO*

The state is propagated at a 60-second rate using the truth NRHO trajectory and environment models provided in Table 3 and the bestrand tracking schedule is used to schedule XNAV observations. The estimated states are the NRHO position, velocity, clock bias, clock bias rate, clock bias acceleration, and solar radiation pressure coefficient. Initialization of the baseline, nominal detector size NRHO simulations uses a basic initialization, with the initial state errors randomly computed based on the following variances and off-diagonal correlation coefficients:

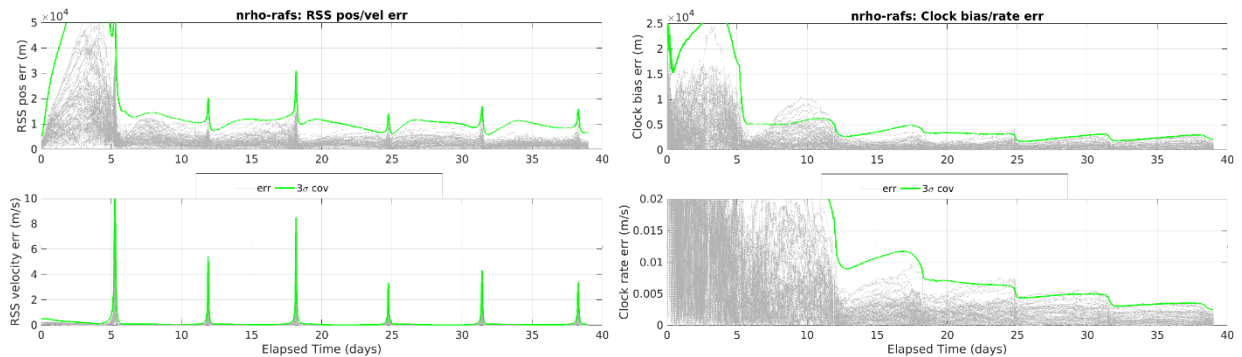
- RIC Position Variances: 1000<sup>2</sup> meters<sup>2</sup> each axis
- RIC Velocity Variances: 0.1<sup>2</sup> meters<sup>2</sup>/sec<sup>2</sup> each axis
- Clock Bias Variance: 10000<sup>2</sup> meters<sup>2</sup>
- Clock Bias Rate Variance: 1 meter<sup>2</sup>/sec<sup>2</sup>
- Clock Bias Acceleration Variance:  $(3 \times 10^{-7})^2$  meters<sup>2</sup>/sec<sup>4</sup>
- Solar Radiation Pressure Coefficient Variance:  $(0.12)^2$
- Correlation of R Position and I Velocity: -0.95
- Correlation of R velocity and I position: -0.90

Figure 12 shows the visibility along with tracking periods and measurement times for an example NRHO run. Note that there is much longer continuous visibility to XNAV pulsars for the NRHO trajectory than for either the LEO or HI-GEO trajectories.



**Figure 12: Visibility over the NRHO run (high=visible). Red marks on the lines show measurement times.**

Figure 13 shows the performance for a set of 70 Monte Carlo trials for the baseline NRHO configuration with a RAFS quality clock. The position and velocity errors reach steady-state error levels below 10 km and 5 cm/s at apolune after about 3 orbits (19.5 days) of processing. The largest position and velocity errors of up to 10 km and 1 to 10 m/s occur near perilune where the lunar gravitational errors are the largest and 2 *desat* disturbances occur. The clock bias and clock bias rate errors are not highly sensitive to the distance to the Moon. The clock bias also reaches steady state after about 3 orbits of measurement processing, but the clock bias rate is still converging after 6 orbits of measurement processing.



**Figure 13. RSS Position and Velocity Errors (left) and Clock Bias and Rate Magnitude Errors (right) for NRHO Baseline Configuration**

### *Sensitivity Analysis Results for NRHO*

Monte-Carlo simulations were run to evaluate the sensitivity of XNAV performance to the variations in the clock stability (USO, RAFS, no clock). These simulations indicate that the RSS position and velocity steady-state errors at apolune increase by about 30%, the clock bias errors are about 2 times larger, and the clock rate errors are about 8 times larger when the less stable USO is used versus the RAFS clock. Similarly at perilune, the RSS position and velocity steady-state errors increase by about 30% and 50% respectively, the clock bias errors increase by about 50%, and the clock rate errors are about 8 times larger when the less stable USO is used versus the RAFS clock. Comparison

of RAFS performance versus the no clock results indicate that RAFS-related errors are a significant error source in the position and velocity errors at perilune but not at apolune.

Monte-Carlo simulations were run to evaluate the sensitivity of XNAV performance to the variations in detector scaling (7, 14, 28, 56, 112 concentrators) using a *gsinit* initialization procedure, including two 4-hour DSN tracking passes separated by 3.5 days at the start of the simulation. Performance is unstable in simulations with fewer than 14 concentrators; however, performance improves with increasing detector size from ¼ size (14 concentrators) to a 2x (112 concentrator) detector. The NRHO also appears to support a significantly smaller detector down to ¼ size (14 concentrators) and a 2x (112 concentrator) detector provides only a marginal improvement.

## CONCLUSIONS

This paper provides an analysis of XNAV performance for three trajectories: an ISS-like LEO, a Highly Inclined GEO (HI-GEO), and a Lunar-Gateway-like NRHO. Each of these trajectories present a challenging case for the applications of XNAV as compared to a deep space cruise, for example. Each case evaluated XNAV-based navigation *and timing*, i.e., including estimation of clock errors states. Simulations included a baseline case modeling a NICER-like detector with a high-quality RAFS oscillator and then assessed the impact of using a lower grade, but still high-quality USO, as well as a perfect clock. The sensitivity of performance to scaling the detector size down and up was also studied. In the case of small detector sizes, a more accurate XNAV initialization procedure based on an uplinked ground-based navigation state was found to be important for aiding initial convergence of the filter.

The LEO trajectory performance results are consistent with the SEXTANT simulation and on-orbit results. With a NICER-like detector, the baseline LEO simulation indicates that RSS position and velocity errors of 10 km and 10 m/s, or better, are reliably achievable when presented with sufficient visibility to XNAV pulsars. Navigation performance is not sensitive to use of the USO. Time and frequency errors of 3 km and 0.02 m/s are achieved with the RAFS and only somewhat degraded with an USO. Due to the high dynamics and regular Earth occultations, the LEO case is quite sensitive to detector size scaling: performance with a ½ size (28 concentrator) detector is still strong, but with ¼ size and smaller, significantly degrades or fails. However, a 2x (112 concentrator) detector provides only a marginal improvement. With our processing approach, smaller detectors correspond to longer observation times, which does not fit well with LEO specific challenges.

*Due to very high particle background radiation levels, equatorial and low inclination Geosynchronous orbits (GEO) below about 40° are not expected to be practical candidates for application of XNAV.* However, it is perhaps possible that through special techniques (e.g., the use of the high-flux Crab pulsar, greatly extended observation times for MSPs, and background reduction techniques) this application might be enabled. Analysis of the sensitivity of XNAV performance to GEO orbit inclination suggests reasonably good XNAV performance is possible at higher inclination. Therefore, XNAV performance was investigated for a HI-GEO at 75° that spends a significant fraction of its time away from the radiation belts. Baseline simulations indicate that navigation to <10 km and 1 m/s is possible. For the HI-GEO, navigation performance sensitivity to the local clock was found to be minimal, and smaller detectors provide comparable performance down to a ¼ size detector (14 concentrators) and a 2x (112 concentrator) detector provides only a marginal improvement.

Evaluation of XNAV performance for the Lunar-Gateway like NRHO trajectory is perhaps the most interesting case for a new future application. The NRHO provides much longer continuous visibility to XNAV pulsars than either the LEO or HI-GEO but with high perilune dynamics that can be destabilizing to navigation. For the NRHO, performance varies greatly between the (brief) perilune and (long) apolune regions. For the baseline NICER-sized detector, 10 km and 5 cm/s velocity accuracies are achievable at apolune. Due to high dynamics, velocity errors can spike to 1-10 m/s at perilune. Sensitivity of the navigation performance to the clock was observed, although timing is much better with the RAFS than the USO. The NRHO also appears to support a significantly smaller detector down to ¼ size (14 concentrators) and a 2x (112 concentrator) detector provides only a marginal improvement.

## FUTURE WORK

Based on the analysis presented in this paper, areas for future investigation include the following:

***Study additional trajectories:*** Cases to consider include other Lunar orbits, Earth-Sun Lagrange point missions, Earth-Mars transit, Asteroid Belt missions, and other deep space trajectories, where XNAV might have advantages when compared to alternative navigation techniques.

**Investigate sensitivity and impact of initialization error, initialization strategies:** Investigate limits to acceptable magnitudes and covariance structure of initialization errors and/or study alternative initialization procedures, and even consider the possibility of cold-start or autonomous initialization.

**Investigate sensitivity to annual pulsar visibility variation:** Any practical XNAV detector will likely need to avoid pointing too close to the Sun. For near-Earth applications, the Sun occults several of the XNAV MSPs for up to a few months each year depending on their location in the sky. Understanding and mitigating this issue, e.g., by investigating practicality of designing detectors that are able to stare closer to the Sun, or by incorporating additional measurement types in the filter, is an important area for future investigation. The plots below show the 56-concentrator HI-GEO and NRHO for a full year for both the 45° and 35° Sun KOZ. The significant benefit of reducing the KOZ is apparent. Similar behavior is expected for the LEO case.

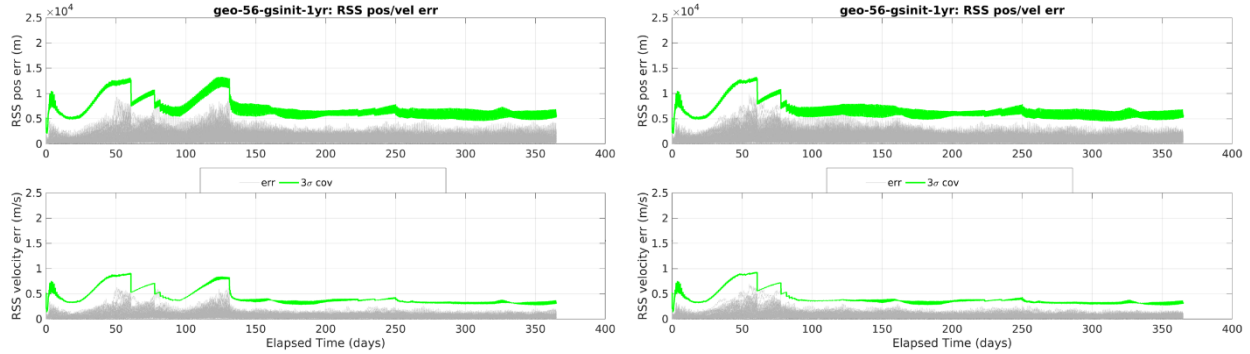


**Figure 14: RSS position and velocity errors for a one-year run of the 56-concentrator HI-GEO case with *gsinit* initialization and 45° solar KOZ (Left) and 35° solar KOZ (Right)**

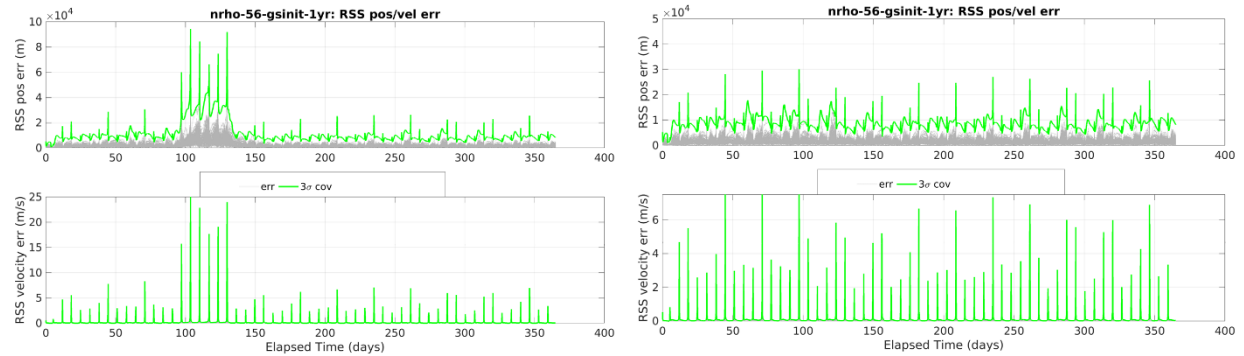


**Figure 15: RSS position and velocity errors for a one-year run of the 56-concentrator HI-GEO case with *gsinit* initialization and 45° solar KOZ (Left) and 35° solar KOZ (Right)**

**Enhancing particle background models and studying background sensitivity:** As described in this paper, we developed new background maps to provide plausible particle background counts for this study. These models used the SPENVIS software together with NICER flight data to try to predict background levels in two very different orbit regimes. Although we believe our models are reasonable, there is still significant uncertainty associated with them. Additional data or analysis could be used to reduce this uncertainty. Furthermore, the current XGMS particle models only apply to the three regimes studied in this paper (although the constant model used in the NRHO might have broader applicability). Developing a general particle background model applicable to a wider range of orbits/trajectories, and e.g., include solar cycle trends, and models of transient solar flare events, would be a valuable addition to the XGMS. It would also be useful to study sensitivity to background levels, which impact both the noise levels in measurement in low to moderate background environments and visibility regions where background levels are high enough to preclude XNAV operation.

**Optimizing MSP target observation times:** The performance of the measurement processing can depend strongly on the selection of the observation time targets for each pulsar under varying background conditions, orbital dynamics,

etc. A detailed investigation of approaches for determining the best observation time for each pulsar would be worthwhile.

***Integration of Crab Pulsar simulation and processing:*** Adding Crab pulsar processing to the XGMS and investigating its use would be a valuable area for future work. The Crab pulsar, *PSR\_B0531+21*, has about 4-5 orders of magnitude larger flux than the XNAV MSPs used in the current XGMS. This means that Crab XNAV measurements can be generated very rapidly within a matter of seconds rather than tens of minutes or hours for other MSPs, which could enhance our present scenarios and open new XNAV applications, including high-dynamic scenarios, etc. The Crab might also remain useful in regions of higher particle background levels. Its dramatic flux difference, however, requires a different approach in simulation and processing due to computational considerations. Unfortunately, the Crab is not a stable clock like the XNAV MSPs used in this study, and so requires frequent updates to its timing models (e.g., on the order of days rather than months or years for MSPs) to maintain a useful level of accuracy for navigation. However, we might speculate that this increased timing model update cadence could be significantly reduced, or even perhaps eliminated, if the GEONS filter were to estimate a bias state or two in the navigation processing.

***Detector concepts, miniaturization, and optimization:*** Studying practical detector concepts for a future XNAV experiment or mission is an important area for future work. A NICER-like detector, even our conceptual scaled-down 14- or 7- concentrator version, might be a relatively large instrument that would not be practical for many possible applications, so miniaturization would be a key goal. Other optimizations for XNAV could include methods for background reduction to mitigate performance degradation in high-particle-background regions, and/or designing the detector to allow reduced solar, and other celestial body, off-pointing constraints, which can have a dramatic impact on performance, as we saw in the analysis above when reducing the Sun KOZ from 45° to 35°.

***Operation in regions of high background:*** Future investigations might explore whether it is possible to operate an XNAV system in application areas with high particle background levels, such as low inclination and equatorial Geosynchronous orbits. If this is possible, it will likely require a combination of techniques including the use of the Crab pulsar, extended and perhaps dynamically optimized observation times for MSPs as well as hardware and software background reduction techniques.

## ACKNOWLEDGEMENT

This research was funded by the National Geospatial-Intelligence Agency and is approved for public release, 22-122. The authors would like to thank Dr. Paul Ray for many helpful discussions.

## REFERENCES

1. Mitchell, J. W., et al., "SEXTANT - Station Explorer for X-ray Timing and Navigation Technology." *AIAA Guidance, Navigation, and Control Conference*. Kissimmee, FL.
2. Arzoumanian, Z., Gendreau, K. C., et al., "The Neutron Star Interior Composition Explorer (NICER): Mission Definition," *Proc. SPIE 9144, Space Telescopes and Instrumentation 2014: Ultraviolet to Gamma Ray*, 914420 (29 July 2014); <https://doi.org/10.1117/12.2056811>
3. Mitchell, J. W., et al., "SEXTANT X-ray Pulsar Navigation Demonstration: Initial On-Orbit Results", *Annual American Astronautical Society (AAS) Guidance and Control Conference 2018*, Breckenridge, CO.
4. Winternitz, L. M. B., et al., "SEXTANT X-ray Pulsar Navigation Demonstration: Additional On-Orbit Results", *International Conference on Space Operations 2018*. Marseille, France.
5. Winternitz, L. M. B, et al. "X-ray Pulsar Navigation Algorithms and Testbed for SEXTANT", *IEEE Aerospace Conference*, Big Sky, MT, March 2015.
6. Winternitz, L. M. B, et al. "SEXTANT X-Ray Pulsar Navigation Demonstration: Flight System and Test Results", *IEEE Aerospace Conference*, Big Sky, MT, March 2016.
7. <https://www.spennis.oma.be/>
8. Vette, J. I., The AE-8 Trapped Electron Model Environment, *NSSDC/WDC-A-R&S 91-24*, 1991a.
9. Sawyer, D. M., and Vette, J. I., AP-8 Trapped Proton Environment for Solar Maximum and Solar Minimum, *NSSDC/WDC-A-R&S 76-06*, 1976.
10. Golshan, A.R, and S. I. Sheikh, S. I., On pulse phase estimation and tracking of variable celestial X-ray sources. In *Proceedings of the 63<sup>rd</sup> Annual Meeting of The Institute of Navigation*, pages 413-422, Cambridge, MA, April 2007. Institute of Navigation.
11. Ashby, N. and Golshan, A. R., Minimum uncertainties in position and velocity determination using X-ray photons from millisecond pulsars. In *Institute of Navigation National Technical Meeting, 2008*.
12. Emadzadeh, A. A., and Speyer, J. L., *Navigation in Space by X-ray pulsars*. Springer, 2011.
13. Hobbs, G. B., Edwards, R. T., Manchester, R. N., TEMPO2, a new pulsar-timing package – I. An overview, *Monthly Notices of the Royal Astronomical Society*, Volume 369, Issue 2, June 2006, Pages 655–672, <https://doi.org/10.1111/j.1365-2966.2006.10302.x>
14. Bar-David, I. Communication under the Poisson Regime. *Information Theory, IEEE Transactions on*, 15(1):31-37, Jan 1969.
15. Steven T. Hutsell, et al., "Operational Use of the Hadamard Variance in GPS", *Proceedings of the 28th Annual Precise Time and Time Interval Systems and Applications Meeting/Proceedings of the Institute of Navigation GNSS+*, pages 201–214, December 1996
16. Spectratime RAFS datasheet, [https://www.spectratime.com/uploads/documents/ispace/iSpace\\_RAFS\\_Spec.pdf](https://www.spectratime.com/uploads/documents/ispace/iSpace_RAFS_Spec.pdf)
17. Okajima, T., et al., The Performance of NICER flight x-ray concentrator. *Proc. SPIE 9905, Space Telescopes and Instrumentation 2016: Ultraviolet to Gamma Ray*, 99051H (22 July 2016).
18. [https://naif.jpl.nasa.gov/pub/naif/misc/MORE\\_PROJECTS/DSG/](https://naif.jpl.nasa.gov/pub/naif/misc/MORE_PROJECTS/DSG/)